

N₂-Plasma-Induced CN-Vacancies in NiCoFe PBAs Enhance Selective Oxygen Evolution Electrocatalytic Performance in Alkaline Seawater

Fei Ma, Chao Wang, Yutong An, Yajie Liu, Xiaorong Xin, Kaicai Fan, Lei Wang, Guanjun Chen,* Zhiqiang Hu,* and Tianrong Zhan*



Cite This: *Inorg. Chem.* 2025, 64, 11165–11176



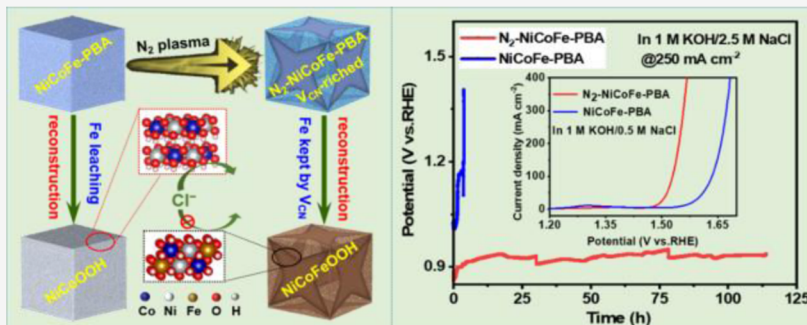
Read Online

ACCESS |

Metrics & More

Article Recommendations

Supporting Information



ABSTRACT: Cheap and advanced electrocatalysts for the oxygen evolution reaction (OER) are vitally significant but challenging for seawater electrolysis. Herein, a glow discharge N₂ plasma is used to etch the [Fe(CN)₆]⁴⁻ group of the NiCoFe Prussian blue analogue (PBA) framework by highly reactive nitrogen radicals (the catalyst named N₂-NiCoFe-PBA). Abundant CN vacancies (V_{CN}) generated by this etching effectively suppress the Fe loss from N₂-NiCoFe-PBA, while the lack of V_{CN} results in the Fe leaching from the NiCoFe-PBA precursor during the anodic process. Consequently, N₂-NiCoFe-PBA and NiCoFe-PBA are transformed into real active phases of NiCoFeOOH and NiCoOOH during the OER process, respectively. Theoretical calculations display that NiCoFeOOH has superior adsorption capacity toward OH⁻ over Cl⁻ to NiCoOOH, which is beneficial to excellent OER activity and anticorrosion performance in alkaline seawaters. In alkaline simulated and natural seawater, N₂-NiCoFe-PBA exhibits much better OER performance with smaller η_{100} (293 and 323 mV) than NiCoFe-PBA (405 and 434 mV). N₂-NiCoFe-PBA can run stably over 110 h in an alkaline high-salty electrolyte (1 M KOH + 2.0 M NaCl) at 250 mA cm⁻². This study provides a modification method without destroying the structure to develop efficient and stable OER catalysts for seawater electrolysis.

1. INTRODUCTION

Hydrogen (H₂) is recognized as an ideal energy carrier due to its high caloric value of 142 MJ/kg and zero-carbon emissions. Renewable electricity-driven seawater splitting has emerged as a promising and sustainable approach for producing green hydrogen,¹ as it effectively harnesses intermittent electrical energy and abundant seawater resources.^{2–4} However, this energy conversion technique will face additional issues due to the presence of high-concentration chloride anions in seawater.^{5,6} For example, the oxidation of chloride (Cl⁻) anions to either chlorine (Cl₂) or hypochlorous acid (HClO) under acidic and alkaline conditions, respectively, on the anode can impair the efficiency of oxygen evolution reaction (OER), which is the bottleneck half-reaction of water splitting.^{7–9} According to Dionigi et al., proposed design criterion,^{10,11} a lower overpotential than 480 mV for an anodic electrocatalyst can selectively achieve 100% seawater oxidation under alkaline conditions. Besides, the aggressive Cl⁻ anions in seawater can destroy the efficient reaction by eroding the anodic catalysts.^{12,13} Consequently, it is crucial to develop efficient

and stable OER catalysts based on transition metals for seawater electrolysis.

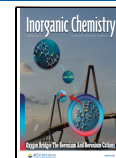
Prussian blue analogues (PBAs) represent a kind of perovskite-type porous compound expressed by a general formula of A_xM[Fe(CN)₆]_y·mH₂O ($y < 1$, $0 < x < 2$), in which A and M are alkali metals and transition metals, respectively.^{14,15} Recently, PBAs have emerged as promising catalysts or precatalysts for the oxygen evolution reaction (OER), attributed to their distinctive porous architectures and abundant redox active sites. However, their inherent limitations, including poor electrical conductivity, moderate interior catalytic activity, and insufficient stability, significantly

Received: April 2, 2025

Revised: May 14, 2025

Accepted: May 23, 2025

Published: May 29, 2025



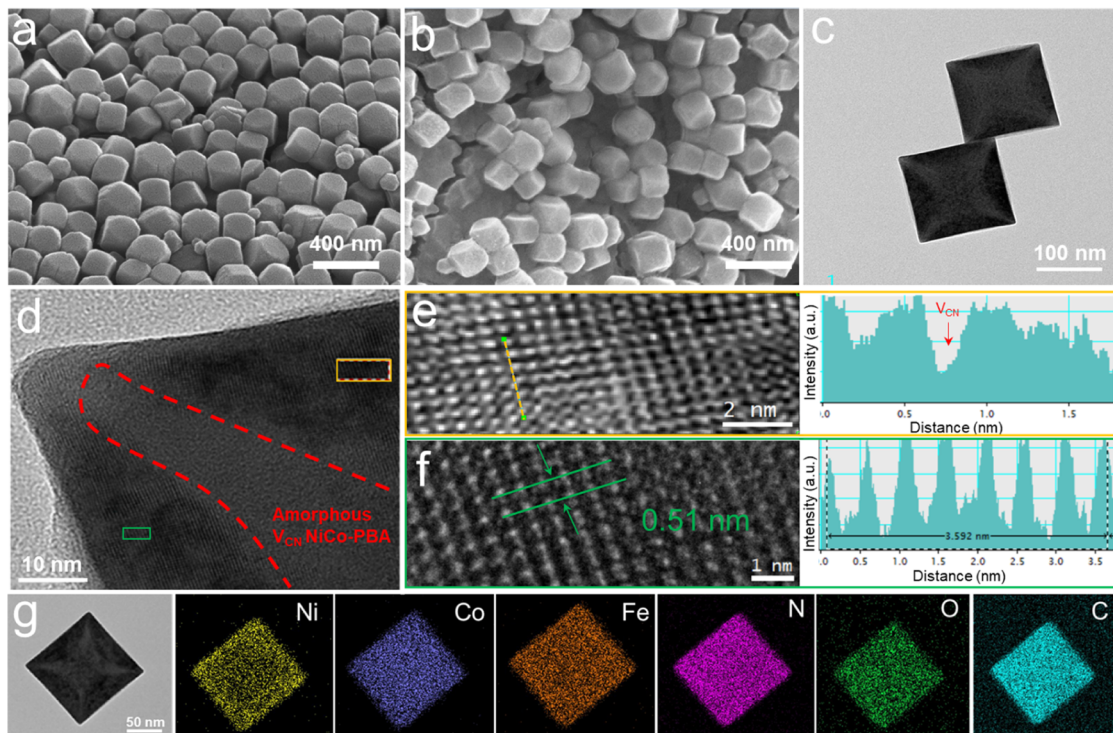
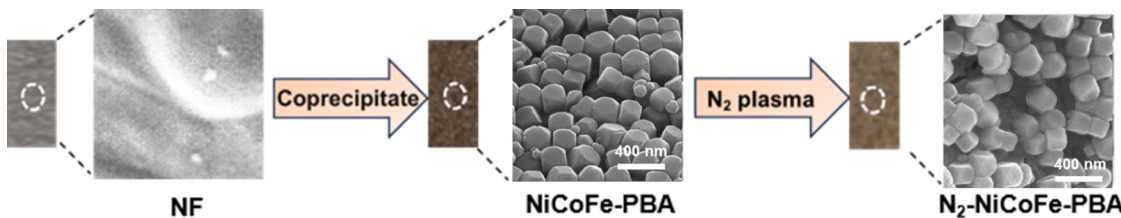
Scheme 1. Schematic Illustration for the Synthesis of N₂-NiCoFe-PBA

Figure 1. SEM images of (a) NiCoFe-PBA and (b) N₂-NiCoFe-PBA. (c) TEM images of N₂-NiCoFe-PBA. (d) HRTEM images of N₂-NiCoFe-PBA. Amplified images and their atomic intensity profiles of the yellow zone (e) and blue zone (f) in d. (g) The corresponding EDS element mapping images of N₂-NiCoFe-PBA.

hinder their practical application in alkaline environments, whether for freshwater or seawater oxidation.^{15,16} Accordingly, PBAs have usually been transformed into oxides, phosphides, and sulfides by pyrolysis at high temperatures.^{16,17} Nonetheless, this modification mode can give rise to the complete damage of PBA frameworks and the loss of the good distribution of metal sites. The manipulation of defects is another effective approach to adjusting the catalytic performance of electrocatalysts. Therefore, the vacancy induced by a nondestructive modification is the most common and readily tailored defect, which can not only tune the local electronic environment but also maintain the original structure of crystal materials, thus enhancing catalytic activity and stability.¹⁸ Many works have demonstrated that plasma-induced hyperactive ions can break the metal-cyano coordination bond and release open metal sites.^{19,20} Additionally, plasma-induced V_{CN} in the catalyst suppresses Fe leaching during the OER and facilitates FeOOH formation.¹⁵ The resulting FeOOH further optimizes the electronic structure, enhances OH⁻ adsorption, and suppresses Cl⁻ adsorption in alkaline seawater, thereby enhancing reaction kinetics.²¹ Despite some exciting achievements, the previous reports mainly focus on the bimetallic PBAs (NiFe or CoFe) as alkaline OER electrocatalysts for

freshwater, but the trimetallic PBAs with CN vacancies (V_{CN}) and their alkaline OER performance for seawater have not been recorded.

Herein, we employ a glow-discharge N₂ plasma to activate the metal sites by creating V_{CN} in the NiCoFe-PBA framework. Owing to its ultrafast and hyperactive nature, the N₂ plasma can realize the selective modification of NiCoFe-PBA without destroying the PBA framework. The modified catalyst (denoted N₂-NiCoFe-PBA) will be reconstructed to NiCo_{0.9}FeOOH during the anodic reaction owing to the preservative role of V_{CN} on the Fe species. Relatively, NiCoFe-PBA without V_{CN} will be transformed into NiCoOOH due to the leaching of the Fe component. The conservation of the Fe species will endow N₂-NiCoFe-PBA with favorable OER kinetics, enhanced selective adsorption toward OH⁻ over Cl⁻, and improved anticorrosive performance in alkaline seawater electrolytes. Electrochemical and structural characterizations and theoretical calculations will be systematically conducted to elucidate the significant effect of the N₂ plasma treatment on NiCoFe-PBA on its OER performance in alkaline seawaters.

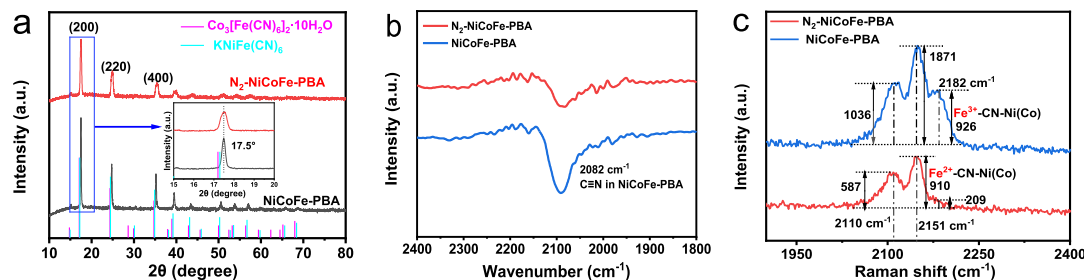


Figure 2. (a) XRD patterns, (b) FT-IR spectra, and (c) Raman spectra of NiCoFe-PBA and N₂-NiCoFe-PBA.

2. RESULTS AND DISCUSSION

2.1. Morphological and Structural Characterization.

The trimetallic cyanide framework (NiCoFe-PBA) was first in situ synthesized on NF by a conventional precipitation method. Then, the yellow-green N₂-NiCoFe-PBA electrode with V_{CN} was fabricated via N₂-plasma bombardment of the purple NiCoFe-PBA precursor at 800 V for 10 min (Scheme 1 and Figure S1). The morphologies of the obtained catalysts were first characterized through scanning electron microscope (SEM). As shown in Figure 1a, NiCoFe-PBA shows uniformly distributed nanocubes in sizes of about 200 nm with sharp corners and edges. After an N₂-plasma activation, N₂-NiCoFe-PBA preserved the nanocube morphology well, but their edges became indistinct and surfaces got rougher than the pristine NiCoFe-PBA (Figure 1b). It is reported that the plasma-induced highly energetic N₂ radicals can cleave Fe–C and Ni(or Co)–N bonds in Fe–CN–Ni(or Co) units, but cannot break the stronger C≡N bond (893 kJ mol⁻¹), thus the formed CN⁻ escapes away from the PBA lattices accompanying the formation of V_{CN}.¹⁹ In addition, the interior part of the cubes is preferentially etched because of their looser structure and higher defect density than the compact exterior surface.²² Consequently, N₂-NiCoFe-PBA presents the nanocage structure with a crystalline–amorphous structure along the diagonal of the PBA nanocages compared to the intact cubic morphology of the NiCoFe-PBA precursor (TEM images in Figures 1c and S2). In this structure, the crystalline and amorphous interfaces provide high conductivity and plentiful unsaturated coordination sites, enabling rapid electron transfer and abundant active sites.^{23–25} Therefore, the crystalline–amorphous structure can boost the OER process by adjusting the interfacial electronic structure and optimizing the adsorption energy.²⁶ In the HRTEM image of N₂-NiCoFe-PBA, the crystalline domain in the yellow zone exhibits a discontinuous atomic configuration and the peak valleys of the atomic intensity spectrum (Figure 1d,e), revealing the generation of V_{CN} by ionized N₂ radicals. The blue zone shows crystalline features with a continuous atomic array and even lattice spacing (~0.51 nm) of the (200) plane of NiFe-PBA or CoFe-PBA^{27,28} (Figure 1f). The photoluminescence (PL) measurements were also carried out to characterize the presence of V_{CN} because vacancy defects can impact the PL properties via the mediated band-to-band transition.²⁹ As shown in Figure S3, N₂-NiCoFe-PBA gives rise to evident PL enhancements against NiCoFe-PBA, possibly because of the high quantum efficiency of excitons localized at the V_{CN} sites. The X-ray spectroscopy (EDS) mappings of N₂-NiCoFe-PBA (Figure 1g) demonstrate a uniform distribution of Ni, Co, Fe, O, C, and N elements in PBA nanocages, indicating well-dispersed metal active sites.

The phase structures of the catalysts were identified by an X-ray powder diffractometer (XRD). In Figure 2a, NiCoFe-PBA exhibits a set of characteristic diffraction peaks of PBA without impurity, indicating a single-phase PBA structure. The standard cards of NiFe-PBA (JCPDS: 51-1897) and CoFe-PBA (JCPDS: 46-0907) display the (200) peaks at 17.3° and 17.2°,^{29–31} respectively. In contrast, NiCoFe-PBA exhibits the (200) peaks at 17.5°, implying that the introduced third metal in binary PBA units would cause a certain degree of lattice shrinking.³¹ After the N₂ plasma treatment, the N₂-NiCoFe-PBA nanocages present the same diffraction lines but with slightly lower intensities and broader peak widths relative to the pristine NiCoFe-PBA. This observation can probably be attributed to the introduction of amorphous defect structures by N₂ plasma.³² The FT-IR and Raman spectra were further analyzed to characterize the structural information of the defect. As displayed in Figure 2b, both NiCoFe-PBA and N₂-NiCoFe-PBA show evident C≡N stretching vibration peaks at ~2082 cm⁻¹.³² However, the peak intensity of C≡N for N₂-NiCoFe-PBA greatly decreases, suggesting that some C≡N groups are removed to form V_{CN} after the N₂ plasma radiation.³² In their Raman spectra (Figure 2c), N₂-NiCoFe-PBA also produces the greatly decreased peak intensities of CN at 2110 and 2151 cm⁻¹ [Fe²⁺–CN–(Ni/Co)^{2+/3+}] and 2182 cm⁻¹ [Fe³⁺–CN–(Ni/Co)²⁺] compared to the NiCoFe-PBA precursor.¹⁹ Meanwhile, the peak strength ratio of 2151 cm⁻¹ to 2110 cm⁻¹ changes from 1.81 to 1.55 after the introduction of V_{CN}, possibly indicating that a part of Ni³⁺ or Co³⁺ gains electrons to transform to Ni²⁺ or Co²⁺. The Raman peak signal at 2182 cm⁻¹ dramatically declines, suggesting a considerable part of Fe³⁺ is reduced to metastable Fe²⁺ in the V_{CN}-rich PBA structure. It has been reported that the formation of V_{CN} can lead to lowered oxidative states of metals in PBAs owing to the removal of electron-rich CN groups.¹⁹ The above results signify that the introduction of V_{CN} can mediate the local electron environment of metallic sites and stabilize metastable metallic species.

X-ray photoelectron spectroscopy (XPS) was used to analyze the chemical states of elements in catalysts. The C 1s spectra of NiCoF-PBA and N₂-NiCoFe-PBA consist of three peaks corresponding to C=C (284.8 eV), C≡N (285.5 eV), and C=O (288.7 eV) (Figure S4a).³³ The N 1s spectra (Figure S4b) only show the broad peak of C≡N at about 398 eV. The intensities of the C≡N species in both C 1s and N 1s for N₂-NiCoFe-PBA are much smaller than those for NiCoFe-PBA, revealing that the N₂ plasma treatment results in the removal of some C≡N bonds from NiCoFe-PBA.³⁴ Based on their XPS survey spectra, the significantly lower contents of C (29.45 at. %) and N (1.73 at. %) for N₂-NiCoFe-PBA than NiCoFe-PBA (C: 48.50 at.%; N: 20.65 at.%) also support the formation of V_{CN} by the N₂ plasma. In Figure S4c, the O 1s

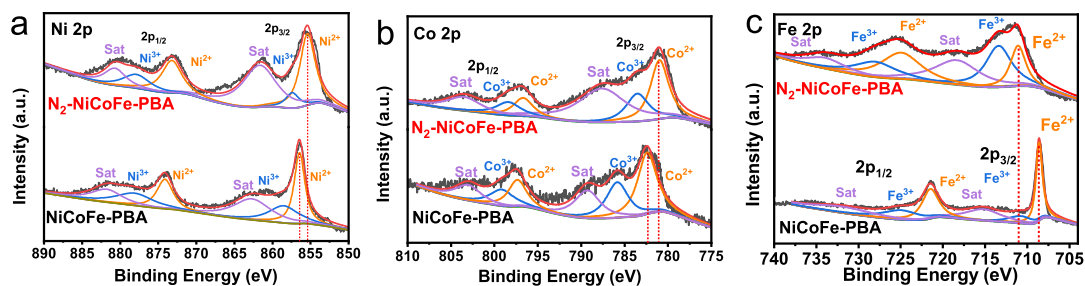


Figure 3. High-resolution XPS spectra of NiCoFe-PBA and N₂-NiCoFe-PBA: (a) Ni 2p, (b) Co 2p, and (c) Fe 2p.

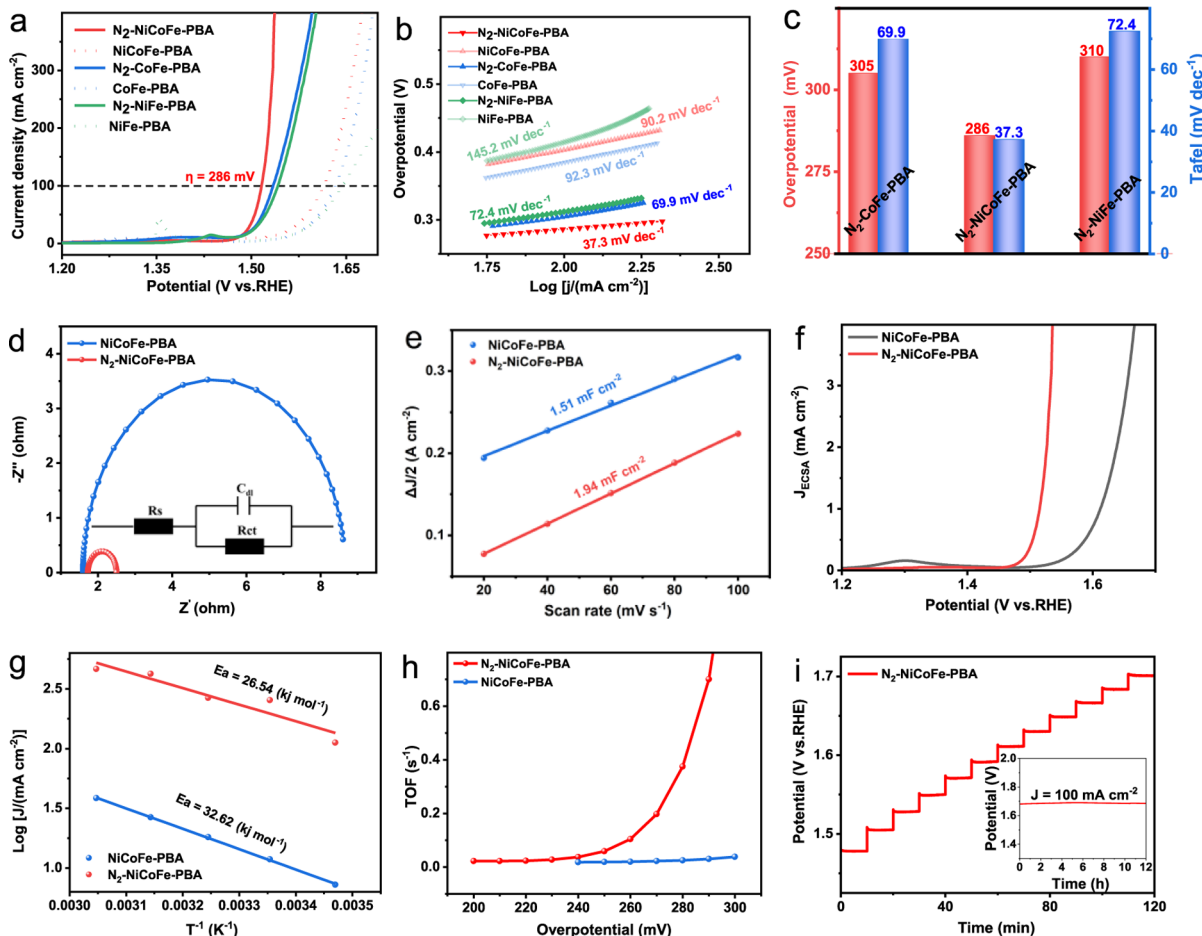


Figure 4. (a) LSV curves and (b) Tafel plots of N₂-NiCoFe-PBA, NiCoFe-PBA, N₂-CoFe-PBA, CoFe-PBA, N₂-NiFe-PBA, and NiFe-PBA. (c) Tafel slopes and η_{100} values of N₂-NiCoFe-PBA, N₂-CoFe-PBA, and N₂-NiFe-PBA. (d) Nyquist plots at 1.523 V (vs RHE), (e) C_{dl} plots, (f) C_{dl}-normalized LSV curves, (g) Arrhenius plots and calculated activation energy, and (h) TOFs based on Ni sites as a function of overpotential of N₂-NiCoFe-PBA, and NiCoFe-PBA. (i) Multistep chronopotentiometric curve of N₂-NiCoFe-PBA. Inset: the OER stability test of N₂-NiCoFe-PBA at 100 mA cm⁻² for 12 h (without iR compensation). The electrolyte is 1.0 M KOH.

spectra of NiCoFe PBA can be deconvoluted into hydroxyl species (M-OH) at 531.7 eV and surface-adsorbed water molecules (H₂O) at 532.5 eV. The N₂ plasma activation results in the appearance of the metal–oxygen bond (M–O) at ~529.0 eV in N₂-NiCoFe-PBA since the strong reaction between the dangling metal sites and the high-energy oxygen species in the air; meanwhile, the M–OH bond has been strengthened, but the water molecule signals become weaker.³² In Figure 3a,b, the Ni 2p spectra are fitted in two spin-orbit Ni 2p_{3/2} and Ni 2p_{1/2} with corresponding shakeup satellites, and the Co 2p spectra are deconvoluted into Co 2p_{3/2} and Co 2p_{1/2} with their shakeup satellites. It can be inferred that the

coexistence of Ni³⁺/Ni²⁺ and Co³⁺/Co²⁺ occurs in both NiCoFe-PBA and N₂-NiCoFe-PBA. Their integral areas disclose that the ratios of Ni³⁺ to Ni²⁺ and Co³⁺ to Co²⁺, respectively, decrease from 0.67 and 0.66 to 0.19 and 0.59 after the N₂-plasma etching toward NiCoFe-PBA, further verifying the reduction of some Ni³⁺ or Co³⁺ to Ni²⁺ or Co²⁺ by V_{CN}. Concerning the Fe 2p spectra (Figure 3c), their peaks shift to higher binding energies. As for the bimetallic NiFe-PBA and CoFe-PBA, the Ni 2p, Co 2p, and Fe 2p spectra follow the same trends in peaks' shifts and the ratios of metallic species. The binding energies of Ni, Co, and Fe in the trimetal-PBAs exhibit shifts to a certain degree compared with those in the

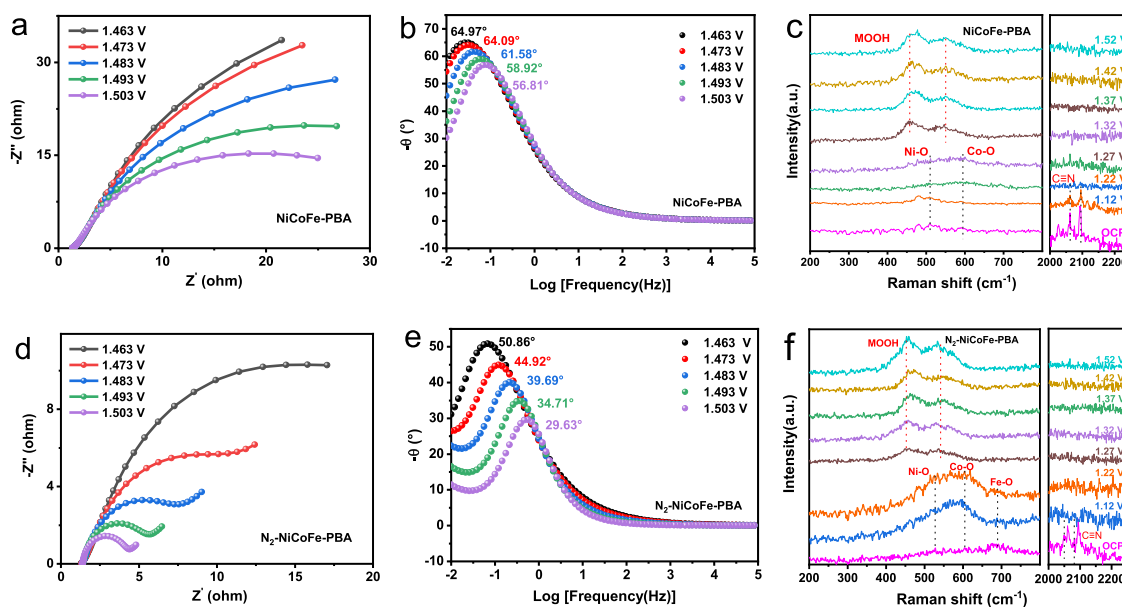


Figure 5. Nyquist and Bode plots, and in situ Raman spectra of (a–c) NiCoFe-PBA and (d–f) N₂-NiCoFe-PBA at different potentials.

bimetal counterparts. The fact shows that there is electronic interaction between the three metal cations, which can advance the OER kinetics (Figure S5). The above discussions uncover that the electron in Fe transfers to Ni and/or Co atoms after the N₂-plasma action toward either trimetallic or bimetallic PBA. It can be concluded that the N₂-plasma irradiation-induced-V_{CN} can adjust the local coordination environments of metallic sites, advancing the OER kinetics.

2.2. Electrocatalytic Performance in Alkaline Freshwater. The electrocatalytic OER performances of the catalysts were evaluated using a three-electrode cell in 1 M KOH electrolyte at room temperature. Initially, we optimized the plasma parameters, including different gas atmospheres (N₂, air, and Ar) and irradiation voltages by LSV, as shown in Figure S6. The optimal plasma conditions were assessed to be the irradiation for 10 min at 800 V under a N₂ atmosphere. Then, the LSV curves with 85% iR correction of different electrocatalysts are collected as shown in Figure 4a. It can be found that, at 100 mA cm⁻², the trimetallic N₂-NiCoFe-PBA and NiCoFe-PBA exhibit overpotentials (η_{100}) of 286 and 385 mV, which are respectively much lower than the corresponding N₂-NiFe-PBA (310 mV) or N₂-CoFe-PBA (305 mV) and NiFe-PBA (415 mV) or CoFe-PBA (404 mV). For comparison, we also determined LSV curves of NiOOH and CoOOH in 1 M KOH. As shown in Figure S7, the OER activities of NiOOH and COOH are pronouncedly inferior to N₂-NiCoFe-PBA. The result reveals that the interactions among trimetallic sites can enhance the OER activity. The strong electronic interactions among the various metal cations result in a synergistic effect that improves the OER activity. Besides, for the three groups of catalysts, the η_{100} values of the N₂-PBA catalysts are 99–117 mV smaller than the corresponding pristine PBA counterparts, emphasizing the crucial contribution of the N₂-plasma treatment to better OER activity. To eliminate the effect of the highly active NF substrate, N₂-NiCoFe-PBA and NiCoFe-PBA powdered catalysts were prepared to modify glassy carbon electrodes (GCE) for LSV measurements in 1 M KOH. N₂-NiCoFe-PBA/GCE visibly outperforms NiCoFe-PBA/GCE (Figure

S8), further demonstrating that the defects (V_{CN}) generated by N₂-plasma are beneficial to the increase in OER activity.

Similarly, the Tafel slopes of the trimetallic N₂-NiCoFe-PBA (37.3 mV dec⁻¹) and NiCoFe-PBA (90.2 mV dec⁻¹) are smaller than the binary catalysts of N₂-NiFe-PBA (72.4 mV dec⁻¹) or N₂-CoFe-PBA (69.9 mV dec⁻¹) and NiFe-PBA (145.2 mV dec⁻¹) or CoFe-PBA (92.3 mV dec⁻¹), respectively (Figure 4b). The Tafel slope of the N₂-PBA sample is also smaller than the corresponding pristine PBA control. The Tafel data further imply that the N₂-plasma-induced V_{CN} and the trimetallic interactions can mutually boost the OER kinetics. Hence, the N₂-NiCoFe-PBA nanocage achieves the best OER activity among the three catalysts (Figure 4c). To explore the influence of V_{CN}, we first investigated the charge transfer of both trimetallic catalysts by EIS, as displayed in Figure 4d. N₂-NiCoFe-PBA presents a substantially smaller charge transfer impedance (R_{ct} : 1.1 Ω) than NiCoFe-PBA (7.4 Ω), revealing that the V_{CN}-enriched PBA nanocages can facilitate charge transfer and OER kinetics. Their ECSA values were estimated using the electrochemical C_{dl} by measuring CV curves at different scan rates under the non-Faraday range (Figure S9). Based on the C_{dl} values in Figure 4e, the ESCAs of N₂-NiCoFe-PBA were calculated to be 48.5 cm⁻², larger than that of NiCoFe-PBA (37.8 cm⁻²), hinting that the crystalline–amorphous structure with abundant V_{CN} releases more active sites.³⁵ The ECSA-normalized LSV curves in Figure 4f also demonstrate that N₂-NiCoFe-PBA has better intrinsic OER activity than NiCoFe-PBA owing to the effect of the N₂-plasma. Their activation energies were assessed by determining the LSV curves at different temperatures (Figure S10). According to the slope of the Arrhenius plot (Figure 4g), a lower barrier energy (26.54 kJ mol⁻¹) was obtained for N₂-NiCoFe-PBA compared with NiCoFe-PBA (32.62 kJ mol⁻¹), indicating that the NiCoFe-PBA nanocages with V_{CN} can improve the intrinsic OER activity. Moreover, N₂-NiCoFe-PBA also has a much higher turnover frequency (TOF) per active site (1.33 s⁻¹ at an overpotential of 300 mV) than NiCoFe-PBA (0.038 s⁻¹) (Figures 4h and S11). All the above results corroborate that introducing V_{CN} into NiCoFe-PBA nanocubes by the N₂-plasma can remarkably enhance the OER

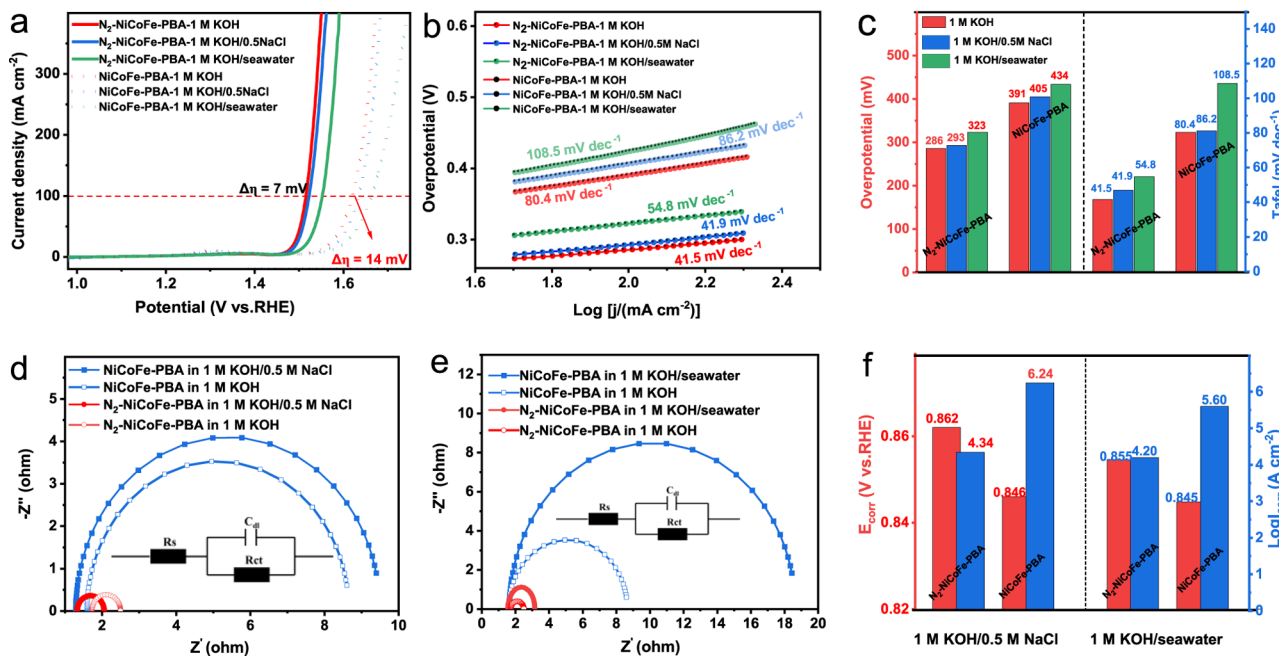


Figure 6. (a) LSV curves, (b) the corresponding Tafel plots, and (c) Tafel slopes and η_{100} values of $\text{N}_2\text{-NiCoFe-PBA}$ and NiCoFe-PBA in 1 M KOH, 1 M KOH/0.5 M NaCl, and 1 M KOH/seawater, respectively. Nyquist plots of $\text{N}_2\text{-NiCoFe-PBA}$ and NiCoFe-PBA at 1.523 V (vs RHE) in (d) 1 M KOH and 1 M KOH/0.5 M NaCl, and (e) 1 M KOH and 1 M KOH/seawater. (f) Corrosion current densities and corrosion potentials of $\text{N}_2\text{-NiCoFe-PBA}$ and NiCoFe-PBA in 1 M KOH/0.5 M NaCl and 1 M KOH/seawater.

kinetics. The $\text{N}_2\text{-NiCoFe-PBA}$ electrode displays excellent stability, which can be evidenced by a multistep chronopotentiometry from 10 to 120 mA cm^{-2} with a fast and stable step-response, and by stable operation over 12 h under a potential of η_{100} value (Figure 4*i*).

2.3. Electrocatalytic Mechanism Analysis. To elucidate the catalytic mechanism, the operando EIS was tested to probe the electrocatalytic kinetics at various potentials during the OER process.³⁶ The high-frequency region stems from surface C_{dl} (the diffusion of OH^- in the surface channel), however, the low-frequency region is associated with the nonhomogeneous charge distribution originating from the electrode surface oxidation during OER.³⁶ As shown in Figure 5*a,d*, Nyquist plots of $\text{N}_2\text{-NiCoFe-PBA}$ and NiCoFe-PBA show two low capacitive responses at different potentials, which were confirmed by their single-phase peaks at the low-frequency region in Bode phase plots (Figure 5*b,e*). In the low-frequency region, $\text{N}_2\text{-NiCoFe-PBA}$ and NiCoFe-PBA display a decreasing trend in the R_{ct} value (indexed by their semicircle diameters) with increasing applied potential. $\text{N}_2\text{-NiCoFe-PBA}$ has much lower R_{ct} values than NiCoFe-PBA at the same potential, indicating faster charge-transfer kinetics during the OER. In their Bode plots, $\text{N}_2\text{-NiCoFe-PBA}$ shows a clear decrease and shift of phase angles compared with NiCoFe-PBA , suggesting a fast conversion of adsorbed OH^- and intermediates.³⁷

The stability of $\text{N}_2\text{-NiCoFe-PBA}$ in 1 M KOH was first evaluated by ex situ Raman spectra (Figure S12).³⁸ $\text{N}_2\text{-NiCoFe-PBA}$ reveals the disappearance of the CN stretching peak and the appearance of the Ni–O and Co–O vibrations after immersion in 1 M KOH for 30 min, nevertheless, it retains almost equal characteristics after immersion in pure water. It is indicative that $\text{N}_2\text{-NiCoFe-PBA}$ is likely to evolve into the corresponding hydroxides in strong alkaline conditions. Afterward, in situ Raman spectroscopy was carried

out to probe the surface reconstruction of $\text{N}_2\text{-NiCoFe-PBA}$ and NiCoFe-PBA during OER. The Raman spectra were recorded at an applied voltage ranging from the open circuit potential (OCP) to 1.52 V vs RHE (Figure 5*c,f*). The peak at a range of 2050–2100 cm^{-1} corresponds to the characteristic CN peak in NiCoFe-PBAs .³³ As the applied potential increases, the distinctive peak of CN disappears at 1.12 and 1.22 V (vs RHE) for $\text{N}_2\text{-NiCoFe-PBA}$ and NiCoFe-PBA , respectively. This observation implies that the defective CN groups in the N_2 -plasma etched sample are more easily replaced by OH^- during the electrochemical reconstruction at a lower potential.¹⁹ $\text{N}_2\text{-NiCoFe-PBA}$ exhibits Ni–O (~525 cm^{-1}), Co–O (~620 cm^{-1}), and Fe–O (~690 cm^{-1}) vibration^{39,40} at OCP ~1.22 V (vs RHE), whereas NiCoFe-PBA shows only the two peaks of Ni–O and Co–O at OCP ~1.27 V (vs RHE), further confirming the formation of FeOOH in $\text{N}_2\text{-NiCoFe-PBA}$ by the N_2 -plasma. Impressively, $\text{N}_2\text{-NiCoFe-PBA}$ presents the E_g bending (471 cm^{-1}) and the A_{1g} stretching (544 cm^{-1}) vibrations in MOOH (NiCoFeOOH) at a lower potential (1.27 V vs RHE) than NiCoFe-PBA (1.32 V vs RHE).⁴⁰ For $\text{N}_2\text{-NiCoFe-PBA}$, the Fe–O vibration at ~690 cm^{-1} disappears at higher potentials than 1.22 V (vs RHE) because FeOOH is unstable at the high potential in an alkaline condition.⁴¹ It can be speculated to be transformed from Ni(OH)_2 and Co(OH)_2 , and partial Fe enters the NiCoOOH lattice due to the break of the Fe–O bond.⁴² These results strongly reveal that the plentiful vacancies and nanocage structure endowed by the N_2 -plasma can facilitate the reconstruction of $\text{N}_2\text{-NiCoFe-PBA}$ to the real active phase MOOH of OER in an anodic environment.

We next conducted “post-mortem” XPS investigations of NiCoFe-PBA and $\text{N}_2\text{-NiCoFe-PBA}$ after the stability test for 24 h at 100 mA cm^{-2} (Figure S13). For NiCoFe-PBA , the Fe 2p spectrum of the postcatalyst only shows the Fe 2p_{3/2} peak at a higher binding energy position (~713 eV), revealing the

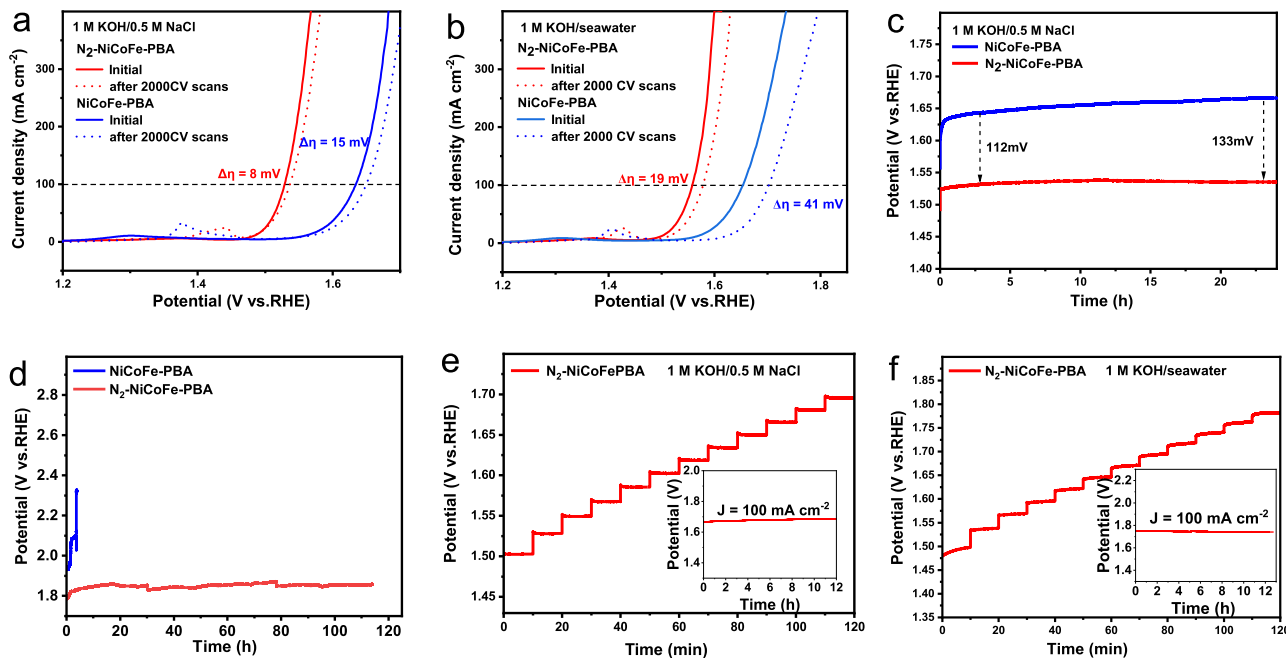


Figure 7. LSV curves of $\text{N}_2\text{-NiCoFe-PBA}$ and NiCoFe-PBA before and after 2000 CV scans in (a) 1 M KOH/0.5 M NaCl and (b) 1 M KOH/seawater. Chronopotentiometric curves of $\text{N}_2\text{-NiCoFe-PBA}$ and NiCoFe-PBA in (c) 1 M KOH/0.5 M NaCl at 100 mA cm^{-2} and (d) 1 M KOH + 2.0 M NaCl at 250 mA cm^{-2} . Multistep chronopotentiometric curves of $\text{N}_2\text{-NiCoFe-PBA}$ in (e) 1 M KOH/0.5 M NaCl and (f) 1 M KOH/seawater without iR compensation (insets are the corresponding chronopotentiometric curves at 100 mA cm^{-2}).

main presence of the Fe^{3+} species.⁴³ The Co 2p peaks shift toward the lower energy side, and the Ni 2p peaks move to the higher energy direction. Furthermore, the Ni/Fe ratio increases from 1.11 to 1.50, indicative of the distinct reduction of the Fe content. The N 1s profile of the post-NiCoFe-PBA also shows the almost disappearance of the CN peak. The above analyses manifest that the ferrocyanide ions ($[\text{Fe}(\text{CN})_6]^{4-}$) in PBA were exchanged with OH^- during the anodic process,^{44,45} leading to the leaching of $[\text{Fe}(\text{CN})_6]^{4-}$ ions and the formation of NiCoOOH .^{46,47} By contrast, for $\text{N}_2\text{-NiCoFe-PBA}$, the characteristic peaks of the Fe 2p, Co 2p, Ni 2p, and N 1s experienced an inappreciable change after the same stability test. The good structural stability of $\text{N}_2\text{-NiCoFe-PBA}$ can be assigned to their abundant V_{CN} , which can create plentiful coordinatively unsaturated Fe sites owing to the decreased Fe–C coordination numbers. In this fashion, these open metallic sites are prone to bond with oxygen atoms to form Fe–O bonds during OER, which thus effectively suppresses the loss of Fe species into the electrolyte.¹⁹ As a result, $\text{N}_2\text{-NiCoFe-PBA}$ was reconstructed into NiCoFeOOH , but NiCoFe-PBA was transformed into NiCoOOH . In addition, as shown in ex situ Raman spectra (Figure S14), the vibration of $\text{C}\equiv\text{N}$ at about 2080 cm^{-1} in $\text{N}_2\text{-NiCoFe-PBA}$ disappears after the OER test; meanwhile, the diffraction peaks of MOOH appear, indicating that $\text{N}_2\text{-NiCoFe-PBA}$ has transformed into NiCoFeOOH , accompanied by the formation of V_{CN} . These surface reconstructions were also supported by the XRD patterns of the two postelectrodes. As illustrated in Figure S15, both of them exhibit only the signals of the NF substrate, suggesting that both catalysts transformed into an amorphous or low-crystalline structure after the anodic process. The morphologies were also determined by SEM to analyze the surface reconstruction (Figure S16). NiCoFe-PBA evolved into an overlayer with numerous distinct cracks after the stability test, in which the NiCoFe-PBA nanocubes

collapsed into interconnected nanosheets. Impressively, the post- $\text{N}_2\text{-NiCoFe-PBA}$ catalyst presents a dense film comprising closely packed hollow nanocages, which can boost OER kinetics by offering more active sites and fast mass/electron transfer.

2.4. Electrocatalytic Performance in Alkaline Seawater. Considering the significance of seawater electrolysis, we also measured their OER performance in alkaline simulated and natural seawater. The LSV curves of NiCoFe-PBA and $\text{N}_2\text{-NiCoFe-PBA}$ in three electrolytes (1 M KOH, 1 M KOH/0.5 M NaCl, and 1 M KOH/seawater) are shown in Figure 6a. $\text{N}_2\text{-NiCoFe-PBA}$ gives rise to much smaller η_{100} values in three different electrolytes (286, 293, and 323 mV) with narrower gaps (7 and 37 mV) than NiCoFe-PBA (391, 405, and 434 mV) with wider ones (14 and 43 mV). $\text{N}_2\text{-NiCoFe-PBA}$ also presents a smaller Tafel slope in three different electrolytes (41.5, 41.9, and 54.8 mV dec^{-1}) than the corresponding value for NiCoFe-PBA (80.3, 86.2, and $108.5 \text{ mV dec}^{-1}$), and the Tafel slope variation of $\text{N}_2\text{-NiCoFe-PBA}$ is smaller than NiCoFe-PBA (Figure 6b,c). The smaller η_{100} values and Tafel slopes disclose the superior OER catalytic activity and kinetics of $\text{N}_2\text{-NiCoFe-PBA}$. Their narrower η_{100} and Tafel slope differences between freshwater and seawater highlight the stronger tolerance toward Cl^- anions, even in natural seawater, than NiCoFe-PBA.³ The η_{100} values of $\text{N}_2\text{-NiCoFe-PBA}$ in alkaline freshwater (286 mV) and simulated seawater (293 mV) are better than or comparable to many reported NiFe-based catalysts (Table S1). The poorer activities in seawater are associated with the degradation of both catalysts by microbes and complex components in natural seawater.¹³ The charge transfer ability of $\text{N}_2\text{-NiCoFe-PBA}$ in seawater was also examined by EIS (Figure 6d). $\text{N}_2\text{-NiCoFe-PBA}$ gives two almost identical R_{ct} values in 1 M KOH ($\sim 0.72 \Omega$) and 1 M KOH/0.5 M NaCl ($\sim 0.76 \Omega$), while NiCoFe-PBA exhibits a larger R_{ct} value in 1 M KOH/0.5 M NaCl ($\sim 8.36 \Omega$) than in 1

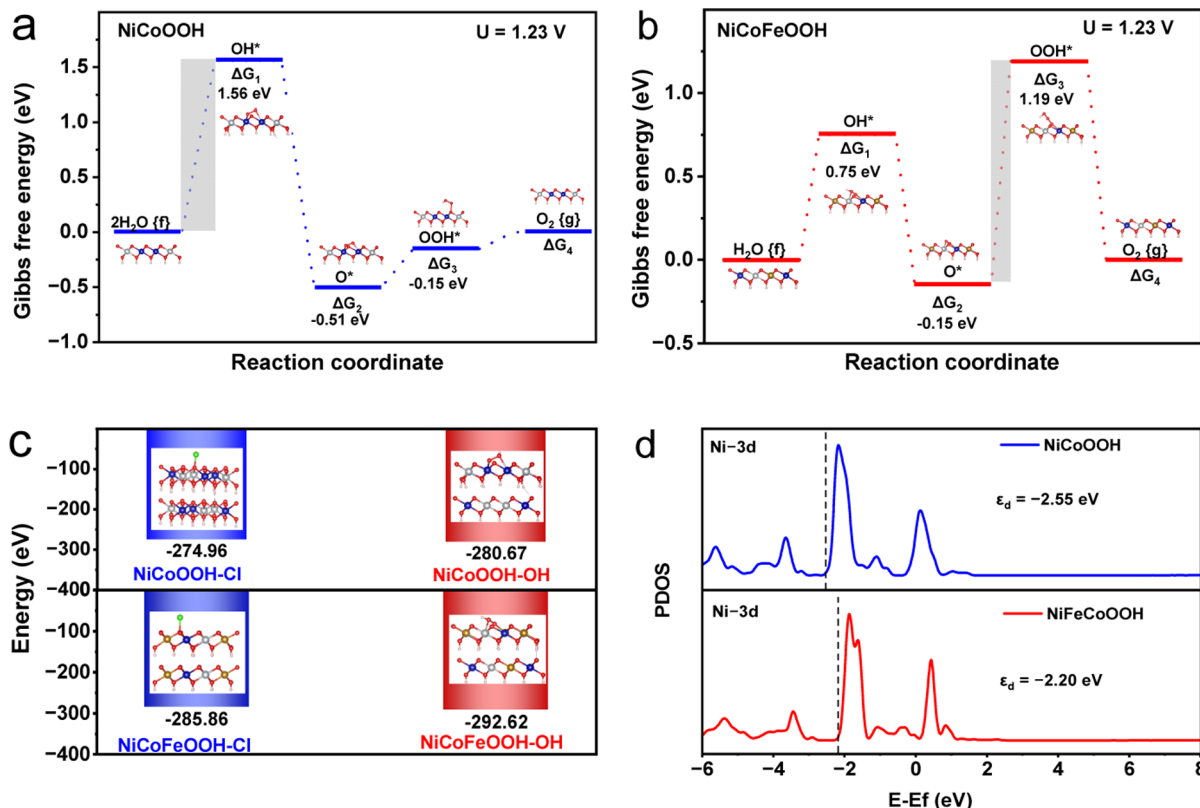


Figure 8. Gibbs free energies for OER of (a) NiCoOOH and (b) NiCoFeOOH models at $U = 1.23$ V. (c) The adsorption energies of NiCoOOH and NiCoFeOOH toward Cl^- and OH^- . (d) PDOS of NiCoOOH and NiCoFeOOH regarding the Ni 3d orbitals.

M KOH ($\sim 6.87 \Omega$). Albeit in the alkaline natural seawater, $\text{N}_2\text{-NiCoFe-PBA}$ presents a closer R_{ct} ($\sim 1.42 \Omega$) to that in 1 M KOH (0.72Ω) than NiCoFe-PBA (6.87 and 16.68Ω) (Figure 6e). These EIS data unveil that $\text{N}_2\text{-NiCoFe-PBA}$ can mitigate the effect of Cl^- anions on charge transfer, since the N_2 -plasma generated V_{CN} can result in an easier reconstruction of the catalyst into NiCoFeOOH rather than NiCoOOH. The inherent corrosion resistances of both catalysts were estimated by corrosion polarization curves in the alkaline simulated and natural seawater (Figures 6f and S17). In both electrolytes, $\text{N}_2\text{-NiCoFe-PBA}$ achieves much smaller corrosion current densities (4.34 and 4.20 mA cm^{-2}) and higher corrosion potentials (0.862 and 0.855 V vs RHE) than NiCoFe-PBA (6.24 and 5.60 mA cm^{-2} , 0.846 and 0.845 V vs RHE), indicating better chloride corrosion resistance.

We now understand that the in situ formed FeOOH can improve corrosion resistance and long-term stability of catalysts in chloride-related environments.⁴⁸ Therefore, the durability of NiCoFe-PBA and $\text{N}_2\text{-NiCoFe-PBA}$ was evaluated by determining their LSV curves after a multicycle CV scan in alkaline seawaters (Figure 7a,b). In the simulated and natural seawaters, $\text{N}_2\text{-NiCoFe-PBA}$ underwent smaller η_{100} increases (8 and 19 mV) than NiCoFe-PBA (15 and 41 mV) after a 2000-cycle CV scan. In addition, in simulated seawater, chronopotentiometry curves demonstrate that $\text{N}_2\text{-NiCoFe-PBA}$ performs more stably than NiCoFe-PBA over 25 h at a current density of 100 mA cm^{-2} (Figure 7c). The accelerated corrosion curves in a high-salt alkaline electrolyte (2.0 M NaCl + 1 M KOH) display that $\text{N}_2\text{-NiCoFe-PBA}$ can run stably over 110 h, whereas the NiCoFe-PBA electrode breaks after only a operation for about 3 h (Figure 7d). Consequently, multistep and single-step chronopotentiometry curves reveal that $\text{N}_2\text{-NiCoFe-PBA}$

displays excellent long-term stability in both alkalized simulated and natural seawater (Figure 7e,f). In addition, no ClO^- was detected using a colorimetric reagent in the 1 M KOH/seawater electrolyte after the CP test for 12 h at 250 mA cm^{-2} on $\text{N}_2\text{-NiCoFe-PBA}$. However, the post-electrolyte for the NiCoFe-PBA becomes blue after experiencing the same CP test (Figure S18). The superior durability and OER selectivity of $\text{N}_2\text{-NiCoFe-PBA}$ in alkaline seawater can be attributed to the formed FeOOH overlayer that can block chloride anions and protect the catalyst from corrosion.⁴⁸ Considering the excellent OER performance, we further determine the Faraday efficiency (FE) of the electrolyzer by employing $\text{N}_2\text{-NiCoFe-PBA}$ as the anode and Pt/C as the cathode in 1 M KOH + seawater at room temperature by a drainage method. As illustrated in Figure S19, the molar ratio of O_2 to H_2 generated on the anode and the cathode is 1:2 during the given period. The FE of this electrolyzer is approaching 100%, indicating that $\text{N}_2\text{-NiCoFe-PBA}$ is an excellent OER-selective electrocatalyst for alkaline seawater splitting. The OH^- adsorption capacity on the electrode surface was evaluated through open-circuit potential (OCP) measurements. As shown in Figure S20, upon the introduction of 5 mM KOH, $\text{N}_2\text{-NiCoFe-PBA}$ delivers a more substantial negative OCP shift (166 mV) than NiCoFe-PBA (103 mV), demonstrating that the $\text{N}_2\text{-NiCoFe-PBA}$ -derived NiCoFeOOH has enhanced adsorption capability for OH^- and better OER selectivity than the NiCoFe-PBA-derived NiCoOOH.

2.5. DFT Calculations. The related density functional theory (DFT) calculations were also conducted to disclose the role of Fe in the PBA catalysts. Since NiCoFe-PBA and $\text{N}_2\text{-NiCoFe-PBA}$ are respectively reconstructed into NiCoOOH

and NiCoFeOOH during the OER process, two theoretical models of NiCoOOH and NiCoFeOOH were built as depicted in Figure S21. The intrinsic OER activities were analyzed by computing the Gibbs free energy (ΔG) profiles on the surfaces of the NiCoOOH and NiCoFeOOH models at a potential of $U = 1.23$ V (Figure S22). The ΔG diagram illustrated in Figure 8a reveals that the rate-determining step (RDS) for NiCoOOH occurs specifically during the formation of the *OH intermediate ($\Delta G = 1.56$ eV) with an overpotential ($\eta = 1.56$ eV). For NiCoFeOOH (Figure 8b), the RDS shifts to the step to form the *OH intermediate ($\Delta G = 0.75$ eV) with a smaller η (1.34 eV). The lowered overpotential implies that the Fe-doped NiCo sites are more beneficial to the OER kinetics owing to a more appropriate adsorption affinity toward OH⁻ than NiCo sites. Figure 8c displays the adsorption energies of Cl⁻ and OH⁻ at Ni surface sites for NiCoOOH and NiCoFeOOH. The data reveal that NiCoOOH and NiCoFeOOH exhibit stronger adsorption capacity toward OH⁻ than Cl⁻. However, relative to NiCoOOH, the adsorption energy of NiCoFeOOH for Cl⁻ affords a smaller reduction (10.90 eV) than that for OH⁻ (11.95 eV), manifesting that the Fe species can improve the OER selectivity and anticorrosion activity of NiCoFeOOH in alkaline seawater electrolytes. Subsequently, we analyzed the projected density of states (PDOS) associated with the Ni 3d orbitals at the adsorption site. As illustrated in Figure 8d, the PDOS mode of NiCoFeOOH presents two peaks at higher energies (-5.4 and -3.4 eV) than NiCoFeOOH (-5.6 and -3.6 eV). The d-band center of NiCoFeOOH for the Ni site ($\epsilon_d = -2.20$ eV) is closer to the Fermi level than that of NiCoOOH ($\epsilon_d = -2.55$ eV), suggesting a stronger bonding of NiCoFeOOH with the OER intermediates. Therefore, the DFT calculations corroborate that the presence of Fe can boost the OER kinetics, and enhance the OER selectivity and corrosion resistance of NiFeCoOOH in alkaline seawater.

3. CONCLUSION

In summary, this work develops a fast surface modification of NiCoFe-PBA by an N₂ plasma, which brings out abundant VCN in the treated PBA of N₂-NiCoFe-PBA. The formed VCN preserves the Fe species in N₂-NiCoFe-PBA, whereas the Fe component in the pure NiCoFe-PBA is leached during the anodic process owing to the absence of VCN. Accordingly, NiCoFe-PBA and N₂-NiCoFe-PBA are reconstructed to NiCoOOH and NiCoFeOOH during the OER, respectively. DFT calculations reveal that the active NiCoFeOOH phase exhibits preferential adsorption toward OH⁻ over Cl⁻ than NiCo sites, thus demonstrating better OER selectivity and anticorrosion activity in alkaline seawater electrolytes. N₂-NiCoFe-PBA shows much smaller η_{100} (293 mV) than NiCoFe-PBA (405 mV) in an alkaline simulated seawater. Even in a high saline–alkaline electrolyte (2.0 M NaCl + 1 M KOH) at a high current density of 250 mA cm⁻², N₂-NiCoFe-PBA also displays much better durability (over 110 h) than NiCoFe-PBA (~3 h).

4. EXPERIMENTAL SECTION

4.1. Materials. All chemical reagents, including nickel nitrate hexahydrate (Ni(NO₃)₂·6H₂O, ≥98%), cobalt nitrate hexahydrate (Co(NO₃)₂·6H₂O, ≥99%), trisodium citrate dihydrate (Na₃C₆H₅O₇·2H₂O, ≥98%) from Sinopharm Chemical Reagent Co., Ltd. (Shanghai, China), and potassium hexacyanoferrate(III) (K₃[Fe(CN)₆], ≥99%) purchased from Aladdin Industrial Corporation

(Shanghai, China), were used as received without further purification. Nickel foam (NF, 3 cm × 2 cm) substrate was obtained from Suzhou Sinero Technology Co., Ltd. Prior to electrode fabrication, the NF substrate underwent sequential ultrasonic cleaning in 3.0 M HCl followed by anhydrous ethanol (15 min each) to remove surface oxides and organic contaminants, followed by copious rinsing with deionized water. Natural seawater collected from Shilaoren Bathing Beach (Qingdao, China) was pretreated through alkalization with 1 M KOH to precipitate Ca²⁺ and Mg²⁺ ions. The resultant suspension was vacuum-filtered through a 0.45 μm membrane, and the collected filtrate was subsequently mixed with 1 M KOH to formulate the alkaline seawater electrolyte.

4.2. Synthesis of NiCoFe-PBA. Ni(NO₃)₂·6H₂O (0.2181 g), Co(NO₃)₂·6H₂O (0.2183 g), and Na₃C₆H₅O₇·2H₂O (0.6617 g) were dissolved in 50 mL of deionized water to generate a clear solution A. Meanwhile, K₃[Fe(CN)₆] (0.3293 g) was dissolved in 50 mL of deionized water to form solution B. The two solutions were then combined via dropwise addition of solution B into solution A under continuous magnetic stirring. Subsequently, the pretreated nickel foam substrate was immersed in the mixed solution and maintained under static conditions for 24 h to allow precursor deposition. Following the reaction, the resultant NiCoFe-PBA composite was sequentially rinsed with deionized water and ethanol (3 cycles each), then dried in a vacuum oven at 50 °C for 12 h to yield the self-supported catalytic electrode.

4.3. Synthesis of N₂-NiCoFe-PBA, N₂-NiFe-PBA, and N₂-CoFe-PBA. The NiCoFe-PBA catalyst was synthesized through N₂ plasma treatment. Specifically, NiCoFe-PBA precursors were subjected to N₂ plasma irradiation for 10 min under controlled conditions: applied voltages ranging from 600 to 900 V (incremental steps of 100 V), a constant current of 0.2 A, N₂ gas flow rate of 30 sccm, and system pressure maintained at 0.8 mbar. For comparative studies, control samples (denoted as Ar-NiCoFe-PBA and Air-NiCoFe-PBA) were prepared under identical plasma parameters using argon and air atmospheres, respectively. The resulting N₂-NiCoFe-PBA catalyst exhibited a controlled mass loading of 0.3 mg cm⁻² as verified by gravimetric analysis (Figure S1). Following the same protocol, binary analogues including N₂-NiFe-PBA and N₂-CoFe-PBA were successfully fabricated to establish composition-dependent catalytic performance comparisons.

4.4. Synthesis of NiOOH and CoOOH. Ni(NO₃)₂·6H₂O (1.163 g) was dissolved in 10 mL of deionized water under continuous magnetic stirring for 10 min, forming a clear solution labeled as solution A. Electrodeposition was performed on a CHI660e workstation with a three-electrode system (NF working, Pt counter, Ag/AgCl (sat. KCl) reference) by cyclic voltammetry from -1.3 to -0.9 V vs Ag/AgCl at 20 mV s⁻¹ for 30 cycles. After the electrodeposition, the electrode was rinsed with deionized water, dried in an oven at 50 °C for 4 h, and then activated in 1 M KOH via cyclic voltammetry (CV) within a potential range of 0.923–1.923 V vs RHE. The activated electrode is denoted as NiOOH. The synthesis of CoOOH followed a procedure similar to that of NiOOH, except that 1.164 g of Co(NO₃)₂·6H₂O was employed.

4.5. Materials Characterizations. XRD was performed on a D8 Advance X-ray diffractometer with Cu K α radiation at a scanning rate of 10° min⁻¹. The structures and morphologies of samples were characterized by a SEM (TESCAN MIRA LMS) and TEM (Titan G2 60-300), equipped with an EDS detector. The FT-IR spectra were recorded on a Thermo Scientific Nicolet iS20 spectrometer in the range of 4000–600 cm⁻¹. Raman spectroscopy was obtained on a HORIBA LabRAM HR Evolution with a 532 nm laser excitation. XPS measurements were taken from the ESCALAB 250XI system using an Al K α X-ray radiation source, and the acquired binding energies were corrected to 284.6 eV for specimen charging as referencing C 1s. Raman spectroscopy was obtained on a HORIBA LabRAM HR Evolution with a 532 nm laser excitation. Photoluminescence (PL) spectra were obtained from a Hitachi F-2700 fluorescence spectrophotometer with an excitation light of 300 nm.

4.6. Electrochemical Measurements. Electrochemical characterizations were conducted using a CHI 660E electrochemical

workstation configured with a standard three-electrode system. The as-synthesized material served as the working electrode, while a Hg/HgO electrode (1 M KOH) and a carbon rod were employed as the reference and counter electrodes, respectively. Three distinct electrolytes were investigated: (i) 1 M KOH, (ii) 1 M KOH + 0.5 M NaCl, and (iii) 1 M KOH + natural seawater. Linear sweep voltammetry (LSV) measurements were performed at a scan rate of 5 mV s⁻¹ with automatic 85% *iR* compensation to obtain polarization curves. To evaluate the electrochemical active surface area (ECSA), CV was carried out within the nonFaradaic potential window of 0.1–0.2 V vs Hg/HgO at varying scan rates (20–100 mV s⁻¹). The double-layer capacitance (C_{dl}) was determined from the slope of the capacitive current difference ($\Delta j = ((+j) - (-j))/2$) versus scan rate plot. ECSA values were subsequently calculated using the relationship $ECSA = C_{dl}/C_s$, where C_s represents the specific capacitance (40 μF cm⁻² for smooth metal surfaces). Tafel analysis was derived from the *iR*-corrected LSV data through linear fitting of the Tafel equation: $\eta = b \log(j) + a$, where η denotes overpotential, b represents the Tafel slope, and j corresponds to current density. Electrochemical impedance spectroscopy (EIS) measurements spanned a frequency range of 0.01 Hz to 100 kHz with an AC amplitude of 5 mV at an applied potential of 1.523 V vs RHE. Long-term stability assessments were performed through chronopotentiometric measurements, maintaining a constant current density of 100 mA cm⁻². All reported potentials were converted to the reversible hydrogen electrode (RHE) scale using the conversion equation: $E(RHE) = E(Hg/HgO) + 0.095 V + 0.0592 \times pH$. 10 mg of catalyst was dispersed in a Nafion solution (concentration: ~10.0 mg mL⁻¹) under 30 min ultrasonication. Subsequently, 5 μL of the resulting ink was drop-cast onto a GCE (3.0 mm diameter) as the working electrode and air-dried.

4.7. TOF Calculations. The surface concentration of Ni active sites (Γ , mol/cm²) was calculated using the equation: slope = $(n^2 F^2 A \Gamma)/(4RT)$, where n is the number of electrons transferred during the oxidation of Ni²⁺ to Ni³⁺ ($n = 1$), F is the Faraday constant, A is the geometrical area of the electrode (1 cm²), R and T represent the universal gas constant and absolute temperature, respectively. The slope was obtained from the linear regression of the oxidation current responses versus scan rate. The number of moles of Ni on the surface participating in the OER, denoted as m , was calculated using the equation: $m = A \times \Gamma$. Finally, the TOF was calculated using the equation: $TOF = jA/(4Fm)$, where j is the current density (A/cm²) of the catalysts at a fixed overpotential, and 4 represents the four-electron transfer process involved in the OER.

4.8. FE Calculation. The FE was determined by comparing experimental and theoretical gas production. FE is calculated as $FE = n_{ex}/n_{th}$, where n_{ex} is the measured moles of oxygen (determined by $n_{ex} = V/V_m$, with V being the gas volume and V_m the molar volume), and n_{th} is the theoretical oxygen yield ($n_{th} = Q/(4F)$, where Q is the total charge and F is Faraday's constant, 96,485 C mol⁻¹) oxygen volume was measured via water displacement.

4.9. DFT Calculations. First-principles DFT calculations were carried out using the Vienna Ab initio Simulation Package (VASP). The exchange–correlation interactions were treated with the Perdew–Burke–Ernzerhof (PBE) formulation of the generalized gradient approximation (GGA). A plane-wave basis set cutoff energy of 400 eV was employed with convergence thresholds of 1×10^{-4} eV for total energy and 0.05 eV Å⁻¹ for atomic forces. Brillouin zone integration was performed using a Monkhorst–Pack *k*-point mesh of $5 \times 3 \times 1$ for structural optimization. For the interfacial heterostructure modeling, we constructed a coherent interface by combining the (001) facet of NiCoFeOOH with the lattice-matched (001) surface of NiCoOOH, ensuring lateral lattice matching through strain optimization. A vacuum layer of 20 Å was introduced perpendicular to the interface plane to eliminate spurious periodic interactions. Atomic positions were fully relaxed except for the bottom two layers to mimic bulk-like constraints. The free energies were calculated using the formula $\Delta G = \Delta E + \Delta ZPE - T\Delta S$, where ΔE represents the total energy obtained from the DFT calculations, ΔZPE denotes the zero-point energy correction, and ΔS accounts for the change in reaction entropy.

ASSOCIATED CONTENT

Data Availability Statement

Data will be made available on request.

Supporting Information

The Supporting Information is available free of charge at <https://pubs.acs.org/doi/10.1021/acs.inorgchem.5c01437>.

Optical image, electrochemical data, structural characterization, and theoretical models of catalysts ([PDF](#))

AUTHOR INFORMATION

Corresponding Authors

Guanjun Chen – School of Materials Science and Engineering, Shaanxi University of Science and Technology, Xi'an 710021, People's Republic of China; Email: sk-cj@ust.edu.cn

Zhiqiang Hu – Key Laboratory of Optic-Electric Sensing and Analytical Chemistry for Life Science (Ministry of Education), College of Chemistry and Molecular Engineering, Qingdao University of Science and Technology, Qingdao 266042, China; orcid.org/0000-0002-6029-3242; Email: huzhiqiang@qust.edu.cn

Tianrong Zhan – Key Laboratory of Optic-Electric Sensing and Analytical Chemistry for Life Science (Ministry of Education), College of Chemistry and Molecular Engineering, Qingdao University of Science and Technology, Qingdao 266042, China; orcid.org/0000-0001-8728-2829; Phone: +86-532-84023927; Email: trzhan@qust.edu.cn

Authors

Fei Ma – Key Laboratory of Optic-Electric Sensing and Analytical Chemistry for Life Science (Ministry of Education), College of Chemistry and Molecular Engineering, Qingdao University of Science and Technology, Qingdao 266042, China; School of Petroleum and Chemical Engineering, Xinjiang Career Technical College, Kuitun 833200, China

Chao Wang – Key Laboratory of Optic-Electric Sensing and Analytical Chemistry for Life Science (Ministry of Education), College of Chemistry and Molecular Engineering, Qingdao University of Science and Technology, Qingdao 266042, China

Yutong An – Key Laboratory of Optic-Electric Sensing and Analytical Chemistry for Life Science (Ministry of Education), College of Chemistry and Molecular Engineering, Qingdao University of Science and Technology, Qingdao 266042, China

Yajie Liu – Key Laboratory of Optic-Electric Sensing and Analytical Chemistry for Life Science (Ministry of Education), College of Chemistry and Molecular Engineering, Qingdao University of Science and Technology, Qingdao 266042, China

Xiaorong Xin – Key Laboratory of Optic-Electric Sensing and Analytical Chemistry for Life Science (Ministry of Education), College of Chemistry and Molecular Engineering, Qingdao University of Science and Technology, Qingdao 266042, China

Kaicai Fan – Key Laboratory of Optic-Electric Sensing and Analytical Chemistry for Life Science (Ministry of Education), College of Chemistry and Molecular Engineering, Qingdao University of Science and Technology, Qingdao 266042, China

Lei Wang – Key Laboratory of Optic-Electric Sensing and Analytical Chemistry for Life Science (Ministry of

Education), College of Chemistry and Molecular Engineering, Qingdao University of Science and Technology, Qingdao 266042, China

Complete contact information is available at:
<https://pubs.acs.org/10.1021/acs.inorgchem.5c01437>

Author Contributions

Fei Ma: Date curation, Investigation, Validation, Writing—original draft. **Chao Wang:** Data curation, Validation, Investigation. **Yutong An:** Investigation. **Yajie Liu:** Investigation. **Xiaorong Xin:** Investigation. **Kaicai Fan:** Supervision. **Lei Wang:** Supervision. **Zhiqiang Hu:** Supervision. **Guanjun Chen:** Date curation, Validation. **Tianrong Zhan:** Conceptualization, Supervision, Writing—review and editing.

Notes

No uncommon hazards are noted.

The authors declare no competing financial interest.

ACKNOWLEDGMENTS

This work is supported by the Natural Science Foundation of Shandong Province, China (Nos. ZR2024MB130, ZR2019MB062, and ZR2014JL013), the Key Research and Development Program of Shandong Province (2017GGX20143), Qingdao New Energy Shandong Laboratory Open Project (QNESL OP202305), and the Shandong Excellent Young Scientists Fund Program (Overseas) (2023HWYQ-091).

REFERENCES

- (1) Qi, H.; Zhang, P.; Wang, H.; Cui, Y.; Liu, X.; She, X.; Wen, Y.; Zhan, T. Cu₂Se Nanowires Shelled with NiFe Layered Double Hydroxide Nanosheets for Overall Water-Splitting. *J. Colloid Interface Sci.* **2021**, *599*, 370–380.
- (2) Zhu, J.; Hu, L.; Zhao, P.; Lee, L. Y. S.; Wong, K.-Y. Recent Advances in Electrocatalytic Hydrogen Evolution Using Nanoparticles. *Chem. Rev.* **2020**, *120* (2), 851–918.
- (3) Wang, Z.; Wang, C.; Ye, L.; Liu, X.; Xin, L.; Yang, Y.; Wang, L.; Hou, W.; Wen, Y.; Zhan, T. MnO_x Film-Coated NiFe-LDH Nanosheets on Ni Foam as Selective Oxygen Evolution Electrocatalysts for Alkaline Seawater Oxidation. *Inorg. Chem.* **2022**, *61* (38), 15256–15265.
- (4) Tan, L.; Wang, H.; Qi, C.; Peng, X.; Pan, X.; Wu, X.; Wang, Z.; Ye, L.; Xiao, Q.; Luo, W.; Gao, H.; Hou, W.; Li, X.; Zhan, T. Regulating Pt Electronic Properties on NiFe Layered Double Hydroxide Interface for Highly Efficient Alkaline Water Splitting. *Appl. Catal., B* **2024**, *342*, 123352.
- (5) Ma, T.; Xu, W.; Li, B.; Chen, X.; Zhao, J.; Wan, S.; Jiang, K.; Zhang, S.; Wang, Z.; Tian, Z.; Lu, Z.; Chen, L. The Critical Role of Additive Sulfate for Stable Alkaline Seawater Oxidation on Nickel-Based Electrodes. *Angew. Chem., Int. Ed.* **2021**, *60* (42), 22740–22744.
- (6) Ye, L.; Ding, Y.; Niu, X.; Xu, X.; Fan, K.; Wen, Y.; Zong, L.; Li, X.; Du, X.; Zhan, T. Unraveling the Crucial Contribution of Additive Chromate to Efficient and Stable Alkaline Seawater Oxidation on Ni-Based Layered Double Hydroxides. *J. Colloid Interface Sci.* **2024**, *665*, 240–251.
- (7) Gao, T.-Q.; Zhou, Y.-Q.; Zhao, X.-J.; Liu, Z.-H.; Chen, Y. Borate Anion-Intercalated NiV-LDH Nanoflakes/NiCoP Nanowires Heterostructures for Enhanced Oxygen Evolution Selectivity in Seawater Splitting. *Adv. Funct. Mater.* **2024**, *34* (24), 2315949.
- (8) Song, Y.; Zhang, X.; Xiao, Z.; Wang, Y.; Yi, P.; Huang, M.; Zhang, L. Coupled Amorphous NiFeP/Crystalline Ni₃S₂ Nanosheets Enables Accelerated Reaction Kinetics for High Current Density Seawater Electrolysis. *Appl. Catal., B* **2024**, *352*, 124028.
- (9) Peng, Z.; Zhang, Q.; Qi, G.; Zhang, H.; Liu, Q.; Hu, G.; Luo, J.; Liu, X. Nanostructured Pt@RuO_x Catalyst for Boosting Overall Acidic Seawater Splitting. *Chin. J. Struct. Chem.* **2024**, *43* (1), 100191.
- (10) Dionigi, F.; Reier, T.; Pawolek, Z.; Gliech, M.; Strasser, P. Design Criteria, Operating Conditions, and Nickel–Iron Hydroxide Catalyst Materials for Selective Seawater Electrolysis. *ChemSusChem* **2016**, *9* (9), 962–972.
- (11) Tong, W.; Forster, M.; Dionigi, F.; Dresp, S.; Sadeghi Erami, R.; Strasser, P.; Cowan, A. J.; Farràs, P. Electrolysis of Low-Grade and Saline Surface Water. *Nat. Energy* **2020**, *5* (5), 367–377.
- (12) Yu, L.; Zhu, Q.; Song, S.; McElhenny, B.; Wang, D.; Wu, C.; Qin, Z.; Bao, J.; Yu, Y.; Chen, S.; Ren, Z. Non-Noble Metal-Nitride Based Electrocatalysts for High-Performance Alkaline Seawater Electrolysis. *Nat. Commun.* **2019**, *10* (1), S106.
- (13) Wang, H.; Chen, L.; Tan, L.; Liu, X.; Wen, Y.; Hou, W.; Zhan, T. Electrodeposition of NiFe-Layered Double Hydroxide Layer on Sulfur-Modified Nickel Molybdate Nanorods for Highly Efficient Seawater Splitting. *J. Colloid Interface Sci.* **2022**, *613*, 349–358.
- (14) Zhang, J.; Yu, L.; Chen, Y.; Lu, X. F.; Gao, S.; Lou, X. W. Designed Formation of Double-Shelled Ni–Fe Layered-Double-Hydroxide Nanocages for Efficient Oxygen Evolution Reaction. *Adv. Mater.* **2020**, *32* (16), 1906432.
- (15) Aguilà, D.; Prado, Y.; Koumousi, E. S.; Mathonière, C.; Clérac, R. Switchable Fe/Co Prussian Blue Networks and Molecular Analogues. *Chem. Soc. Rev.* **2016**, *45* (1), 203–224.
- (16) Cao, L.-M.; Lu, D.; Zhong, D.-C.; Lu, T.-B. Prussian Blue Analogues and Their Derived Nanomaterials for Electrocatalytic Water Splitting. *Coord. Chem. Rev.* **2020**, *407*, 213156.
- (17) Wang, L.; Wang, J.; Yan, L.; Ding, Y.; Wang, X.; Liu, X.; Li, L.; Ju, J.; Zhan, T. Prussian Blue Analogue-Derived Iron Sulfide–Cobalt Sulfide Nanoparticle-Decorated Hollow Nitrogen-Doped Carbon Nanocubes for the Selective Electrochemical Detection of Dopamine. *ACS Sustain. Chem. Eng.* **2022**, *10* (51), 17230–17240.
- (18) Lai, C.; Li, H.; Sheng, Y.; Zhou, M.; Wang, W.; Gong, M.; Wang, K.; Jiang, K. 3D Spatial Combination of CN Vacancy-Mediated NiFe-PBA with N-Doped Carbon Nanofibers Network Toward Free-Standing Bifunctional Electrode for Zn–Air Batteries. *Adv. Sci.* **2022**, *9* (11), 2105925.
- (19) Yu, Z.-Y.; Duan, Y.; Liu, J.-D.; Chen, Y.; Liu, X.-K.; Liu, W.; Ma, T.; Li, Y.; Zheng, X.-S.; Yao, T.; Gao, M.-R.; Zhu, J.-F.; Ye, B.-J.; Yu, S.-H. Unconventional CN Vacancies Suppress Iron-Leaching in Prussian Blue Analogue Pre-Catalyst for Boosted Oxygen Evolution Catalysis. *Nat. Commun.* **2019**, *10* (1), 2799.
- (20) Wang, W.-B.; Cao, H.-J.; Li, G.-L. In Situ Charge Modification within Prussian Blue Analogue Nanocubes by Plasma for Oxygen Evolution Catalysis. *Inorg. Chem.* **2023**, *62* (26), 10241–10248.
- (21) Wang, X.; Chen, J.; Xu, L.; Miao, J.; Sunarso, J.; Wang, X.; Cao, W.; Yang, Y.; Zhou, W. Electrocatalytic Selective Oxygen Evolution of FeOOH-Modified Perovskite for Alkaline Seawater Electrolysis. *J. Power Sources* **2024**, *614*, 235017.
- (22) Mukherjee, P.; Sathiyan, K.; Vishwanath, R. S.; Zidki, T. Anchoring MoS₂ on an Ethanol-Etched Prussian Blue Analog for Enhanced Electrocatalytic Efficiency for the Oxygen Evolution Reaction. *Mater. Chem. Front.* **2022**, *6* (13), 1770–1778.
- (23) Osman, S.; Peng, C.; Li, F.; Chen, H.; Shen, J.; Zhong, Z.; Huang, W.; Xue, D.; Liu, J. Defect-Induced Dense Amorphous/Crystalline Heterophase Enables High-Rate and Ultrastable Sodium Storage. *Adv. Sci.* **2022**, *9* (36), 2205575.
- (24) Zhe, T.; Shen, S.; Li, F.; Li, R.; Li, M.; Ma, K.; Xu, K.; Jia, P.; Wang, L. Bimetallic-MOF-Derived Crystalline–Amorphous Interfacial Sites for Highly Efficient Nitrite Sensing. *Food Chem.* **2023**, *402*, 134228.
- (25) Diao, F.; Kraglund, M. R.; Cao, H.; Yan, X.; Liu, P.; Engelbrekt, C.; Xiao, X. Moderate Heat Treatment of CoFe Prussian Blue Analogues for Enhanced Oxygen Evolution Reaction Performance. *J. Energy Chem.* **2023**, *78*, 476–486.
- (26) Li, D.; Qin, Y.; Liu, J.; Zhao, H.; Sun, Z.; Chen, G.; Wu, D.-Y.; Su, Y.; Ding, S.; Xiao, C. Dense Crystalline–Amorphous Interfacial

- Sites for Enhanced Electrocatalytic Oxygen Evolution. *Adv. Funct. Mater.* **2022**, *32* (7), 2107056.
- (27) Singh, B.; Prakash, O.; Maiti, P.; Indra, A. Electrochemical Transformation of Metal Organic Framework into Ultrathin Metal Hydroxide-(Oxy)Hydroxide Nanosheets for Alkaline Water Oxidation. *ACS Appl. Nano Mater.* **2020**, *3* (7), 6693–6701.
- (28) Shi, W.; Zhu, J.; Gong, L.; Feng, D.; Ma, Q.; Yu, J.; Tang, H.; Zhao, Y.; Mu, S. Fe-Incorporated Ni/MoO₂ Hollow Heterostructure Nanorod Arrays for High-Efficiency Overall Water Splitting in Alkaline and Seawater Media. *Small* **2022**, *18* (52), 2205683.
- (29) Nagaraja, P.; Hemantha Kumar, M. S.; Yathirajan, H. S.; Prakash, J. S. Novel Sensitive Spectrophotometric Method for the Trace Determination of Cyanide in Industrial Effluent. *Anal. Sci.* **2002**, *18* (9), 1027–1030.
- (30) Quan, L.; Li, S.; Zhao, Z.; Liu, J.; Ran, Y.; Cui, J.; Lin, W.; Yu, X.; Wang, L.; Zhang, Y.; Ye, J. Hierarchically Assembling CoFe Prussian Blue Analogue Nanocubes on CoP Nanosheets as Highly Efficient Electrocatalysts for Overall Water Splitting. *Small Methods* **2021**, *5* (7), 2100125.
- (31) Du, M.; Geng, P.; Pei, C.; Jiang, X.; Shan, Y.; Hu, W.; Ni, L.; Pang, H. High-Entropy Prussian Blue Analogues and Their Oxide Family as Sulfur Hosts for Lithium-Sulfur Batteries. *Angew. Chem., Int. Ed.* **2022**, *61* (41), No. e202209350.
- (32) Zhang, W.; Dong, Y.; Huang, M.; Liu, Z. Facile Vacancies Engineering of CoFe-PBA Nanocubes for Enhanced Oxygen Evolution. *J. Alloys Compd.* **2023**, *935*, 168084.
- (33) Liang, X.; Wang, G.; Gu, W.; Ji, G. Prussian Blue Analogue Derived Carbon-Based Composites toward Lightweight Microwave Absorption. *Carbon* **2021**, *177*, 97–106.
- (34) Zhang, J.; Tang, F.; Wan, K.; Yang, Y.; Zhang, C.; Ming, P. W.; Li, B. MOF-Derived CoFe Alloy Nanoparticles Encapsulated within N,O Co-Doped Multilayer Graphitized Shells as an Efficient Bifunctional Catalyst for Zinc–Air Batteries. *J. Mater. Chem. A* **2022**, *10* (28), 14866–14874.
- (35) Li, L.; Sun, H.; Xu, X.; Humayun, M.; Ao, X.; Yuen, M. F.; Xue, X.; Wu, Y.; Yang, Y.; Wang, C. Engineering Amorphous/Crystalline Rod-like Core–Shell Electrocatalysts for Overall Water Splitting. *ACS Appl. Mater. Interfaces* **2022**, *14* (45), 50783–50793.
- (36) Cao, L.-M.; Zhang, J.; Ding, L.-W.; Du, Z.-Y.; He, C.-T. Metal-Organic Frameworks Derived Transition Metal Phosphides for Electrocatalytic Water Splitting. *J. Energy Chem.* **2022**, *68*, 494–520.
- (37) Feng, Y.; Yan, G.; Wang, T.; Jia, W.; Zeng, X.; Sperry, J.; Sun, Y.; Tang, X.; Lei, T.; Lin, L. Synthesis of MCM-41-Supported Metal Catalysts in Deep Eutectic Solvent for the Conversion of Carbohydrates into 5-Hydroxymethylfurfural. *ChemSusChem* **2019**, *12* (5), 978–982.
- (38) Nguyen, T. X.; Yang, K.-H.; Huang, Y.-J.; Su, Y.-H.; Clemens, O.; Xie, R.-K.; Lin, Y.-J.; Lee, J.-F.; Ting, J.-M. Anodic Oxidation-Accelerated Self-Reconstruction of Tri-Metallic Prussian Blue Analogue toward Robust Oxygen Evolution Reaction Performance. *Chem. Eng. J.* **2023**, *474*, 145831.
- (39) Hu, C.; Hu, Y.; Fan, C.; Yang, L.; Zhang, Y.; Li, H.; Xie, W. Surface-Enhanced Raman Spectroscopic Evidence of Key Intermediate Species and Role of NiFe Dual-Catalytic Center in Water Oxidation. *Angew. Chem., Int. Ed.* **2021**, *60* (36), 19774–19778.
- (40) Gao, P.; Zeng, Y.; Tang, P.; Wang, Z.; Yang, J.; Hu, A.; Liu, J. Understanding the Synergistic Effects and Structural Evolution of Co(OH)₂ and Co₃O₄ toward Boosting Electrochemical Charge Storage. *Adv. Funct. Mater.* **2022**, *32* (6), 2108644.
- (41) Zhang, N.; Hu, Y.; An, L.; Li, Q.; Yin, J.; Li, J.; Yang, R.; Lu, M.; Zhang, S.; Xi, P.; Yan, C.-H. Surface Activation and Ni-S Stabilization in NiO/NiS₂ for Efficient Oxygen Evolution Reaction. *Angew. Chem., Int. Ed.* **2022**, *61* (35), No. e202207217.
- (42) Tang, M.; Liu, X.; Ali, A.; He, Y.; Shen, P.; Ouyang, Y. Operando Spectroscopies Capturing Surface Reconstruction and Interfacial Electronic Regulation by FeOOH@Fe₂O₃@Ni(OH)₂ Heterostructures for Robust Oxygen Evolution Reaction. *J. Colloid Interface Sci.* **2023**, *636*, 501–511.
- (43) Naderi, A.; Jourshabani, M.; Asrami, M. R.; Lee, B.-K. Bottom-up Reconstruction and Phase Change over Nickel–Iron Layered Double Hydroxides for Boosted Electrocatalytic Oxygen Evolution Reaction. *Chem. Eng. J.* **2024**, *484*, 149111.
- (44) Chen, Z.; Fei, B.; Hou, M.; Yan, X.; Chen, M.; Qing, H.; Wu, R. Ultrathin Prussian Blue Analogue Nanosheet Arrays with Open Bimetal Centers for Efficient Overall Water Splitting. *Nano Energy* **2020**, *68*, 104371.
- (45) Su, X.; Wang, Y.; Zhou, J.; Gu, S.; Li, J.; Zhang, S. Operando Spectroscopic Identification of Active Sites in NiFe Prussian Blue Analogues as Electrocatalysts: Activation of Oxygen Atoms for Oxygen Evolution Reaction. *J. Am. Chem. Soc.* **2018**, *140* (36), 11286–11292.
- (46) Qiu, L.; Wang, Q.; Yan, P.; Yu, X.-Y. Chemical–Physical Synergistic Etching Enabling Deep Reconstruction of NiFe Prussian Blue Analogue for Efficient Oxygen Evolution Reaction and Zn–Air Batteries. *J. Mater. Chem. A* **2022**, *10* (40), 21251–21259.
- (47) Singh, B.; Prakash, O.; Maiti, P.; Menezes, P. W.; Indra, A. Electrochemical Transformation of Prussian Blue Analogues into Ultrathin Layered Double Hydroxide Nanosheets for Water Splitting. *Chem. Commun.* **2020**, *56* (95), 15036–15039.
- (48) Jiang, K.; Liu, W.; Lai, W.; Wang, M.; Li, Q.; Wang, Z.; Yuan, J.; Deng, Y.; Bao, J.; Ji, H. NiFe Layered Double Hydroxide/FeOOH Heterostructure Nanosheets as an Efficient and Durable Bifunctional Electrocatalyst for Overall Seawater Splitting. *Inorg. Chem.* **2021**, *60* (22), 17371–17378.

CAS BIOFINDER DISCOVERY PLATFORM™

PRECISION DATA FOR FASTER DRUG DISCOVERY

CAS BioFinder helps you identify targets, biomarkers, and pathways

Unlock insights

CAS 
A division of the American Chemical Society